# Solar Cells Using Quantum Funnels

Illan J. Kramer, Larissa Levina, Ratan Debnath, David Zhitomirsky, and Edward H. Sargent*

Department of Electrical and Computer Engineering, University of Toronto, 10 King's College Road, Toronto, Ontario M5S 3G4, Canada

S *Supporting Information*

ABSTRACT: Colloidal quantum dots offer broad tuning of semiconductor bandstructure via the quantum size effect. Devices involving a sequence of layers comprised of quantum dots selected to have different diameters, and therefore bandgaps, offer the possibility of funneling energy toward an acceptor. Here we report a quantum funnel that efficiently conveys photoelectrons from their point of generation toward an intended electron acceptor. Using this concept we build a solar cell that benefits from enhanced fill factor as a result of this quantum funnel. This concept addresses limitations on transport in soft condensed matter systems and leverages their advantages in large-area optoelectronic devices and systems.

KEYWORDS: Depleted heterojunction, colloidal quantum dot, bandgap engineering, photovoltaics, solar cell, quantum funnel
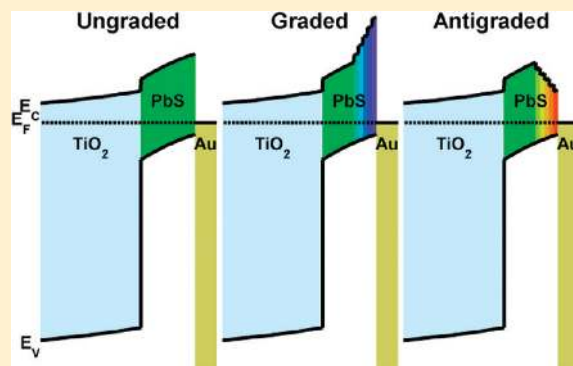
Colloidal quantum dots (CQDs) are attractive for solar energy harvesting[1] and light sensing[2] applications in view of their size-effect tuning across visible and short-wavelength infrared (IR).[3] CQD photovoltaic (PV) devices have recently reached promising power conversion efficiencies (η) of over 5%.[4] Further progress in CQD PV device performance is limited by low electron mobilities[5] that result in short minority carrier diffusion lengths.[6]

We took the view that improved device architecture could help overcome transport limitations in this otherwise highly promising materials system. Our concept was to exploit bandgap engineering within the light-absorbing, charge-transporting CQD active layer to funnel performance-limiting photoelectrons toward the charge-collection TiO₂ electrode.

Bandgap engineering has previously been employed to produce back surface fields in crystalline semiconductors[7,8] and to produce charge transport/blocking layers in organic light-emitting diodes[9] or organic solar cells.[10,11] It has been proposed that bandgap grading can help PV performance through a number of mechanisms and in a variety of materials.[12−16] Solution-processed organic and dye-sensitized PV devices have benefited from innovative strategies employing resonant energy transfer among chromophores with the goal of improving device performance,[17−19] and amorphous compound semiconductors have exploited stoichiometric tuning of one or more of the constituent elements.[20]

In CQDs, quantum size-effect tuning provides an experimentally convenient route to building a photoelectron funnel, or cascade. Figure 1a illustrates a spatial band diagram of a photoelectron cascade within a PV device. The graded structure drives minority electrons, the performance-limiting charge carrier, in the same direction as the built-in electric field formed by the N−p heterojunction at the TiO₂/PbS CQD interface. As controls, we also construct and characterize throughout this work an

ungraded device, which benefits from the built-in N−p junction field alone; and an antigraded device wherein grading opposes electron collection.

In the ungraded device, photons in the red and IR are absorbed not only in the depletion region, but also in the quasi-neutral region. Exciton diffusion lengths have been shown to be shorter than 10 nm in CQD films based on CQD films having the optimal single-junction bandgap.[21] Charge carriers photogenerated in the quasi-neutral region thus fail to reach the edge of the depletion region before they recombine.

In the graded device, an additional driving force for electrons is introduced in what was previously undepleted material. The grading appears primarily in the conduction band for two reasons: for PbS CQDs in the 4−5 nm diameter range, electron affinity varies much more rapidly with CQD diameter than does the ionization potential (Figure 1c).[22] In addition, our use of a p-type semiconductor of uniform doping ensures relatively flat valence bands if the ionization potential of the CQDs were to vary.

We turned to one-dimensional self-consistent modeling of the uniform and graded devices of Figure 1a. The details of our modeling assumptions are provided in Methods. In devices illuminated from the junction side (Figure 2a,c,e,g), striking performance enhancements are obtained for 100−150 nm thick devices at all wavelengths. At the longer wavelengths, such as near the exciton, these originate from enhanced short-circuit current density as minority carriers are harvested within the region that was, in the ungraded device, undepleted.
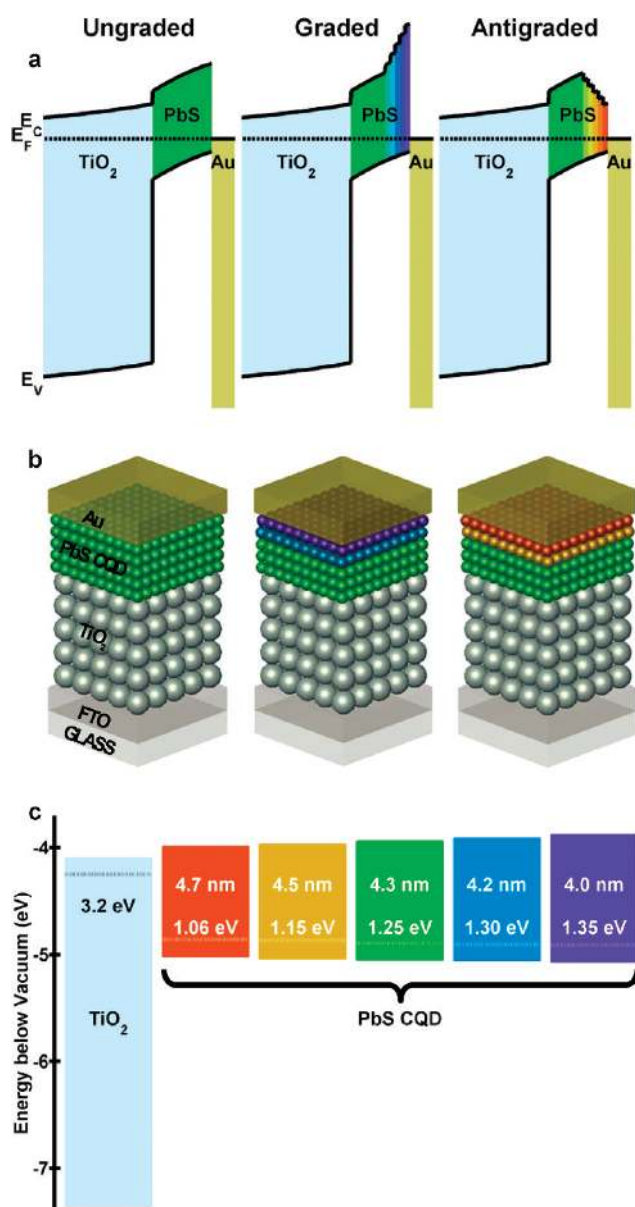
Figure 1. (a) Spatial band diagrams of ungraded, graded and antigraded CQD solar cells. Color coding corresponds to larger bandgaps (more blue/violet) and smaller bandgaps (more yellow/red). (b) Schematic diagram of device cross sections with the same color coding scheme as (a). (c) Detailed band alignment for the TiO_2 and PbS CQD materials used, also employing the same color coding scheme.

Remarkably, at short wavelengths at which light is substantially absorbed inside the depletion region (as it appeared under short-circuit conditions), monochromatic power conversion efficiency is enhanced nevertheless. This manifests as an enhancement in fill factor (Figure 3b inset) instead of short-circuit current density. The impact of grading is greater still in modeled devices illuminated from the ohmic side (Figure 2b,d, f,h), where the visible portion of the spectrum rather than the IR is most strongly absorbed far from the N−p heterojunction. More complete characterization of the optimal quantum funnel is shown in the Supporting Information (Figures SI1-1, SI1-2).

Quantum grading is particularly experimentally accessible in view of the layer-by-layer technique widely practiced in CQD device fabrication.[23,24] In our graded devices, solutions containing smaller-diameter CQDs (Figure 3a) are employed to build the upper layers. The spatial band diagrams of Figure 1a depict, to scale (both in space and energy), the constituent CQDs selected to model each of the three classes of devices, while the physical devices (Figure 1b) were fabricated using the materials consistent with Figure 1c.

PV performance under 1 sun illumination (Figure 3b) shows that fill factor is enhanced in the graded device compared to the ungraded. Under short-circuit conditions, the device is nearly fully depleted[4] and therefore the electric field acts upon all photogenerated carriers throughout the thickness of the device. As the device is biased toward open-circuit conditions, the energy bands flatten out as the magnitude of the electric field is reduced. A quasi-neutral region grows further inward from the back of the device, degrading carrier extraction. The graded device ensures that minority carriers generated at these depths continue to be driven to the electron-accepting TiO_2 even when reverse-bias is reduced under operating conditions. This translates into successful maintenance of a high current, more closely approaching the short-circuit current density, even as power is delivered to a load and the maximum power point is approached. This is manifest in a desirably increased shunt resistance (Figure 3c) that dominates the improvement in fill factor.

The trend of improving performance with the graded architecture was confirmed over seven data sets, yielding an average fill factor improvement to $54 \pm 4\%$ (graded) compared to $49 \pm 4\%$ (ungraded). The short-circuit current density remains essentially unchanged at 12.1 ± 2.8 mA/cm^2 (graded) vs 12.4 ± 3.7 mA/cm^2 (ungraded). The reduction in performance due to antigrading was confirmed over three data sets, yielding an average fill factor reduction down to $37 \pm 9\%$ (antigraded) compared to $49 \pm 4\%$ (ungraded). Short-circuit current was reduced to 8.2 ± 1.7 mA/cm^2 (antigraded) compared to 12.4 ± 3.7 mA/cm^2 (ungraded). Figure 3c shows a single such representative data set.

The benefits of quantum grading are not only confined to devices exhibiting solar power conversion efficiencies of 2−3% but can similarly improve performance of high-efficiency devices as shown through modeling (Supporting Information, Figure SI2-1). In order to achieve the best efficiencies on an ungraded device, the individual performance of each constituent layer needs to be optimized. While this was done on the 950 nm excitonic peak devices previously reported,[4] full optimization is needed for each of the constituent layers of the quantum funnel devices discussed herein.

We now present photoluminescence spectroscopy aimed at verifying independently the proposed minority carrier funneling mechanism. The following two control devices are included: ungraded versions made up entirely of the smallest-gap, and of the largest-gap, CQD films that make up the graded device. These provide reference spectra for comparison with PL from the graded device. The photoluminescence spectra show that, when illuminated from its large-bandgap side, the graded device emits photoluminescence exclusively from its small-bandgap CQDs. In sum, photoelectrons are successfully funneled into the small-gap layers. We modeled this same effect, using the same electronic materials parameters as employed in Figure 2. As seen in Figure 4a (top), recombination in the graded device occurs in the small-bandgap layers though generation is in the large-gap layers. These experiments were conducted without applied bias and therefore at
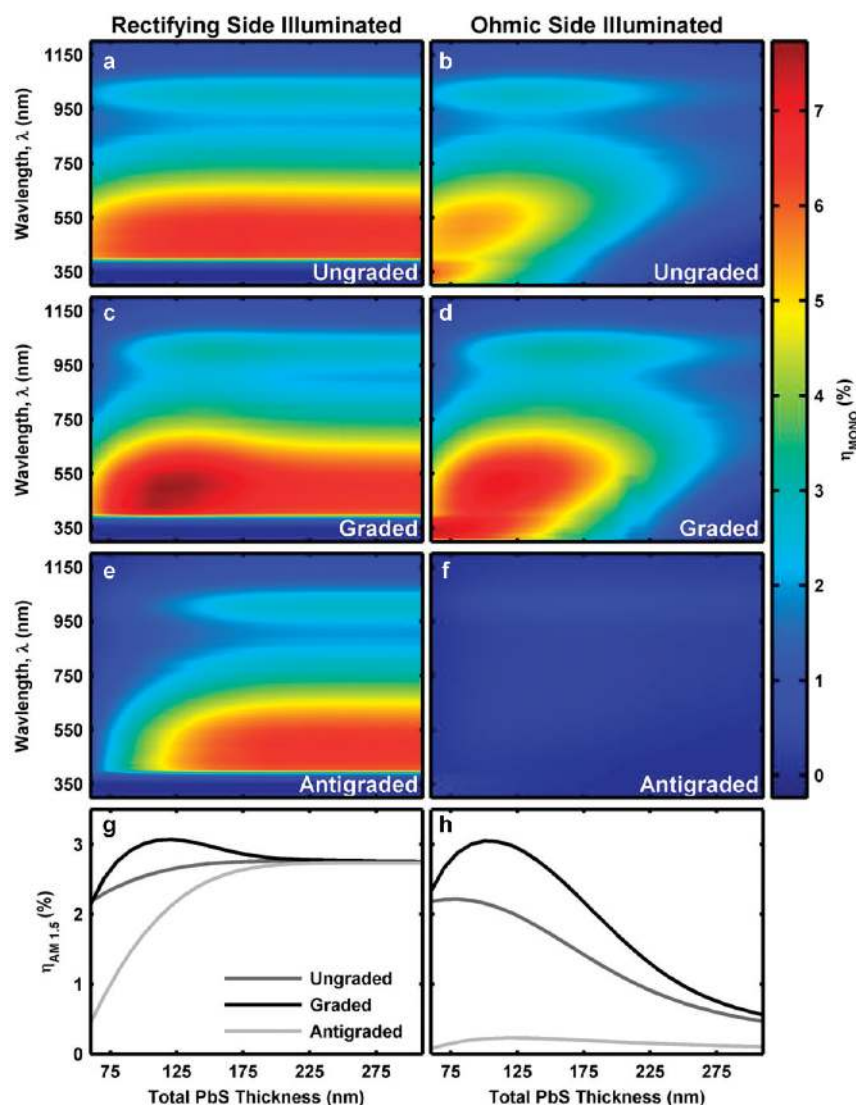
Figure 2. (a–f) Monochromatic power conversion efficiency (η_{MONO}) of ungraded (a,b), graded (c,d), and antigraded (e,f) devices as a function of different PbS CQD thicknesses and illumination wavelength. (g,h) Solar AM 1.5 power conversion efficiency of the three structures as a function of PbS CQD thickness. In panels a, c, e, and g, illumination is from the rectifying side of the device (i.e., through TiO_2). In panels b, d, f and h, illumination is through the ohmic top contact and the bottom contact is made to be a reflective metal instead of FTO. The surface mappings of panels c and d show that maximum η_{MONO} can be achieved at approximately 120 nm thick PbS films, which also maps to the thickness at which the best AM 1.5 power conversion efficiency ($\eta_{AM\ 1.5}$) can be achieved. Furthermore, panels c and d show a widening of the light blue band around 1000 nm compared to panels a and b indicating enhanced charge extraction associated with more weakly absorbed photons that generate photocarriers deeper inside the device.

open-circuit conditions, where the valence band is approximately flat throughout the CQD layer while the grading appears in the conduction band.[22] This enables holes to diffuse without impediment and recombine with minority electrons, the latter being the recombination-limiting carrier. It should be noted that the design of this experiment does not, on its own distinguish between exciton funneling[25] and electron funneling. However, the improvement in collection efficiency in the reverse-biased CQD PV devices suggests that the electric field in a growing depletion region, and thus electron and hole drift-based transport, plays a leading role in carrier extraction in CQD PV.

We show via the SEMs of Figure 4b that our layer-by-layer process keeps each CQD layer compositionally distinct, rather than producing intermixing. The bottom five layers of this structure include 4.3 nm CQDs, followed by single layers of each

of 4.2 and then 4.0 nm CQDs, terminated by two top 4.3 nm layers (not a meaningfully graded structure, but instead one intended to focus on resolving layers in SEM). The different bandgap materials provide different shades of gray,[26] the two darkest layers corresponding to the largest-bandgap CQDs.

Measured external quantum efficiency (EQE) and absorption spectra (Figure 4c) further elucidate the mechanism of device improvement. The absorption spectra confirm that the graded device possess no more absorption than the ungraded one. EQE spectra for all graded and ungraded devices are the same in visible wavelengths (within measurement error) where photons are largely absorbed within the depletion region. The antigraded device, however, has somewhat reduced performance even at these visible wavelengths because in this device the quantum funnel contributes a driving force for photoelectrons toward the
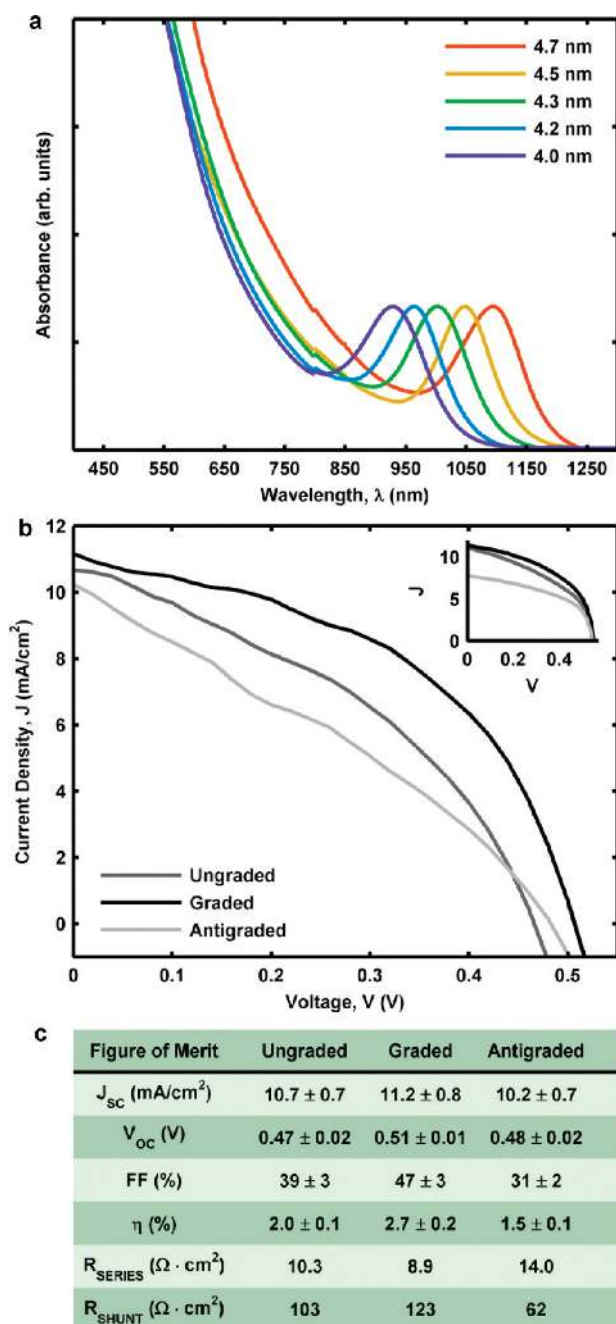
Figure 3. (a) Normalized solution absorption spectra of the five PbS CQD sizes used to make the ungraded, graded, and antigraded devices. Line colors are as in Figure 1c. (b) Current−voltage performance under AM 1.5 conditions of the ungraded, graded, and antigraded devices indicating the increase in fill factor as the dominant mechanism for improvement in η. The inset shows modeled $J-V$ curves for optimal 120 nm device thickness. (c) Summary of PV performance parameters for the three fabricated devices. The improvement in performance is characterized by a modest improvement in current along with a major improvement in fill factor, driven by a nearly 20% increase in shunt resistance.

back contact. This competition has an even more obvious deleterious impact, as expected, in the IR, where fewer photons are absorbed within the depletion region. Furthermore, the near identical EQE (short-circuit conditions) performance of the graded and ungraded devices across all wavelengths further reinforces the conclusion that grading's primary impact is on fill factor.

For materials with short minority carrier diffusion lengths, including present-day CQD films, amorphous semiconductors, and organic semiconductors, photoelectron cascades provide conditions for efficient collection of photogenerated carriers even from regions of the device not having a sufficiently extended depletion region. The benefits to power conversion efficiency are dominated by an improved fill factor. CQDs, with their easy-to-modify bandgaps and layer-by-layer solution processing, provide an ideal platform in which to implement such a photoelectron funnel.

Methods. One-dimensional models were prepared using SCAPS 3.0.00 employing CQD absorption coefficients and doping densities based on measured values. Electron affinities were based on literature values.[22] Each graded layer had a thickness of 10 nm while the principal absorbing layer thickness varied to achieve the total PbS thickness illustrated in Figure 2.

PbS CQDs were synthesized using a variation on a literature method.[27] TiO_2 electrodes were prepared from a commercially available TiO_2 paste (DSL-90T, Dyesol, Inc.) on SnO_2/F-coated glass substrates (Pilkington TEC 15, Hartford Glass, Inc.). CQD films were prepared on TiO_2 electrodes by multilayer spincoating of 37.5 mg·mL^{-1} solution in octane under ambient conditions. Each layer was deposited at 2500 rpm and treated briefly with 10% 3-mercaptopropionic acid in methanol also spin-cast at 2500 rpm; each layer was then rinsed with methanol while spinning at 2500 rpm. The ungraded device consists of five layers of 4.3 nm PbS CQDs, the graded device consists of three layers of 4.3 nm PbS CQDs with subsequent layers of 4.2 and 4.0 nm PbS CQDs and the antigraded device consists of three layers of 4.3 nm of PbS CQDs with subsequent layers of 4.5 and 4.7 nm PbS CQDs. Each layer is approximately 25 nm resulting in a total device thickness of ∼125 nm. The device was then transferred to a glovebox with N_2 atmosphere and left overnight. Contacts consisting of 15 nm of gold topped with 90 nm of silver were deposited by thermal evaporation at a rate of 0.4 and 1 Å/s, respectively, at a pressure of $<1 \times 10^{-6}$ mbar. Contact sizes were 0.061 cm^2.

$J-V$ data was measured using a Keithley 2400 source-meter under ambient conditions. The solar spectrum at AM1.5 was simulated to within class A specifications (less than 25% spectral mismatch) with a Xe lamp and filters (ScienceTech) with measured intensity at 101 mW cm^{-2}. The source intensity was measured with a Melles-Griot broadband power meter (responsive from 300 to 2000 nm), through a circular 0.049 cm^2 aperture at the position of the sample and confirmed with a calibrated solar cell (Newport, Inc.). The accuracy of the current−voltage measurements was estimated to be ±7%.

The EQE spectrum was obtained by passing the output of a 400W Xe lamp through a monochromator and using appropriate order-sorting filters. The collimated output of the monochromator was measured through a 1 mm aperture with calibrated Newport 818-UV and Newport 818-IR power meters as needed. The beam was optically chopped and cofocused on the pixel with a solar simulator at 1-sun intensity. The measurement bandwidth was ∼40 nm and the intensity varied with the spectrum of the Xe lamp. The current response was measured with a Stanford Research Systems lock-in amplifier across an appropriately small resistor (25 ohms) to approximate short-circuit conditions. The accuracy of the EQE measurements was estimated to be ±8%.
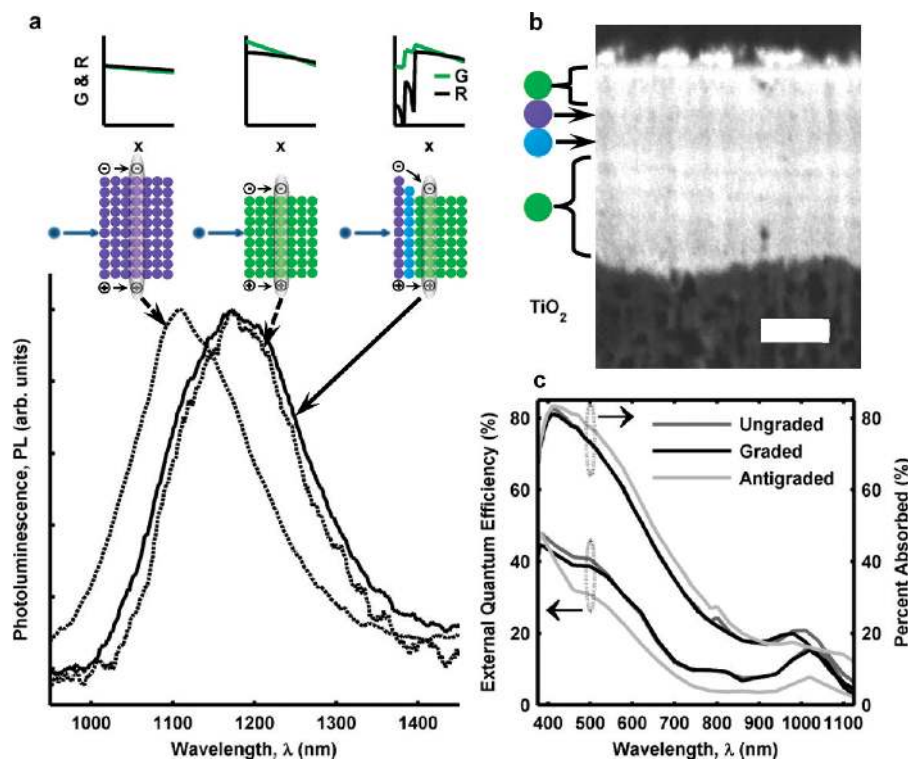
Figure 4. (a) Photoluminescence studies of the largest bandgap CQDs found in the graded structure, the smallest bandgap CQDs found in the graded structure, and a structure whose grading produces a funnel away from the photoexcitation side of the device. The two ungraded samples act as controls that provide the photoluminescence spectra of each class of CQDs in film. The photoluminescence of the graded structure is seen experimentally to overlap closely with the PL spectrum of the small-bandgap material. From this we conclude that photogenerated charge carriers are efficiently funneled to the smallest-bandgap material in the graded film. This is consistent with generation (green) and recombination (black) plots (a, top) of the three structures predicted using the same model and parameters employed in Figure 2. The vertical axes in the modeling results are logarithmic. (b) Focused ion beam scanning electron microscope cross section of an illustrative substrate with two larger bandgap PbS CQDs sandwiched between five layers of small PbS CQDs and another two layers of small PbS CQDs. The thick dark line (referenced by the blue and violet circle indicators) corresponds to the larger bandgap materials. The figure shows that the layer-by-layer process results in distinct layers and thus confirms that the approach can generate bandgap grading instead of simple intermixing. Scale bar is 200 nm. (c) EQE and device absorption curves. The antigraded structure, as expected, converts long wavelengths far less efficiently than do the ungraded and graded devices.

Absorption spectroscopy was carried out using a Cary 500 UV−vis-IR Scan photospectrometer with an attached integrating sphere for film measurements and without for solution measurements. Focused ion beam scanning electron microscopy was conducted at the Canadian Center for Electron Microscopy at McMaster University. Photoluminescence experiments were carried out using an Ocean Optics NIR512 spectrometer coupled to a focusing lens and 1000 nm long pass filter through an optical fiber while simultaneously illuminating the sample with a 428 nm continuous wave laser source.

ASSOCIATED CONTENT

Supporting Information. Discussion and figures. This material is available free of charge via the Internet at http://pubs.acs.org.

AUTHOR INFORMATION

Corresponding Author
*E-mail: ted.sargent@utoronto.ca.

ACKNOWLEDGMENT

REFERENCES

(1) Sargent, E. H. *Nat. Photonics* **2009**, *3*, 325–331.
(2) Konstantatos, G.; Sargent, E. H. *Nat. Nanotechnology* **2010**, *5*, 391–400.
(3) Sargent, E. H. *Adv. Mater.* **2005**, *17*, 515–522.
(4) Pattantyus-Abraham, A. G.; Kramer, I. J.; Barkhouse, A. R.; Wang, X.; Konstantatos, G.; Debnath, R.; Levina, L.; Raabe, I.; Nazeeruddin, M. K.; Grätzel, M.; Sargent, E. H. *ACS Nano* **2010**, *4*, 3374–3380.
(5) Liu, Y.; Gibbs, M.; Puthussery, J.; Gaik, S.; Ihly, R.; Hillhouse, H. W.; Law, M. *Nano Lett.* **2010**, *10*, 1960–1969.

(6) Johnston, K. W.; Pattantyus-Abraham, A. G.; Clifford, J. P.; Myrskog, S. H.; Hoogland, S.; Shukla, H.; Klem, E. J. D.; Levina, L.; Sargent, E. H. *Appl. Phys. Lett.* **2008**, *92*, 122111.

(7) Wolf, M. *Proceedings of the IEEE* **1963**, *51*, 674–693.

(8) von Roos, O. *J. Appl. Phys.* **1978**, *49*, 3503.

(9) Yan, H.; Lee, P.; Armstrong, N. R.; Graham, A.; Evmenenko, G. A.; Dutta, P.; Marks, T. J. *J. Am. Chem. Soc.* **2005**, *127*, 3172–3183.

(10) Peumans, P.; Forrest, S. R. *Appl. Phys. Lett.* **2001**, *79*, 126–128.

(11) Brabec, C. J.; Shaheen, S. E.; Winder, C.; Serdar Sariciftci, N.; Denk, P. *Appl. Phys. Lett.* **2002**, *80*, 1288.

(12) Koeppe, R.; Bossart, O.; Calzaferri, G.; Sariciftci, N. S. *Sol. Energy Mater. Sol. Cells* **2007**, *91*, 986–995.

(13) Morales-Acevedo, A. *Sol. Energy* **2009**, *83*, 1466–1471.

(14) Tsakalakos, L. *Mater. Sci. Eng., R* **2008**, *62*, 175–189.

(15) Weiss, E. A.; Chiechi, R. C.; Geyer, S. M.; Porter, V. J.; Bell, D. C.; Bawendi, M. G.; Whitesides, G. M. *J. Am. Chem. Soc.* **2008**, *130*, 74–82.

(16) Kamat, P. V. *J. Phys. Chem. C* **2008**, *112*, 18737–18753.

(17) Hardin, B. E.; Hoke, E. T.; Armstrong, P. B.; Yum, J.-H.; Comte, P.; Torres, T.; Frechet, J. M. J.; Nazeeruddin, M. K.; Gratzel, M.; McGehee, M. D. *Nat. Photonics* **2009**, *3*, 406–411.

(18) Han, J.-H.; Paulus, G. L. C.; Maruyama, R.; Heller, D. A.; Kim, W.-J.; Barone, P. W.; Lee, C. Y.; Choi, J. H.; Ham, M.-H.; Song, C.; Fantini, C.; Strano, M. S. *Nat. Mater.* **2010**, *9*, 833–839.

(19) Shankar, K.; Feng, X.; Grimes, C. A. *ACS Nano* **2009**, *3*, 788–794.

(20) Guha, S.; Yang, J.; Pawlikiewicz, A.; Glatfelter, T.; Ross, R.; Ovshinsky, S. R. *Appl. Phys. Lett.* **1989**, *54*, 2330.

(21) Choi, J. J.; Lim, Y.-F.; Santiago-Berrios, M. B.; Oh, M.; Hyun, B.-R.; Sun, L.; Bartnik, A. C.; Goedhart, A.; Malliaras, G. G.; Abruña, H. D.; Wise, F. W.; Hanrath, T. *Nano Lett.* **2009**, *9*, 3749–3755.

(22) Hyun, B.-R.; Zhong, Y.-W.; Bartnik, A. C.; Sun, L.; Abruña, H. D.; Wise, F. W.; Goodreau, J. D.; Matthews, J. R.; Leslie, T. M.; Borrelli, N. F. *ACS Nano* **2008**, *2*, 2206–2212.

(23) Klem, E. J. D.; MacNeil, D. D.; Cyr, P. W.; Levina, L.; Sargent, E. H. *Appl. Phys. Lett.* **2007**, *90*, 183113.

(24) Luther, J. M.; Law, M.; Beard, M. C.; Song, Q.; Reese, M. O.; Ellingson, R. J.; Nozik, A. J. *Nano Lett.* **2008**, *8*, 3488–3492.

(25) Klar, T. A.; Franzl, T.; Rogach, A. L.; Feldmann, J. *Adv. Mater.* **2005**, *17*, 769–773.

(26) Perovic, D. D.; Castell, M. R.; Howie, A.; Lavoie, C.; Tiedje, T.; Cole, J. S. W. *Ultramicroscopy* **1995**, *58*, 104–113.

(27) Hines, M. A.; Scholes, G. D. *Adv. Mater.* **2003**, *15*, 1844–1849.